Bulletin of the Seismological Society of America, Vol. 95, No. 3, pp. 995–1010, June 2005, doi: 10.1785/0120030207

Stochastic Finite-Fault Modeling Based on a Dynamic Corner Frequency

by Dariush Motazedian and Gail M. Atkinson

Abstract In finite-fault modeling of earthquake ground motions, a large fault is divided into N subfaults, where each subfault is considered as a small point source. The ground motions contributed by each subfault can be calculated by the stochastic point-source method and then summed at the observation point, with a proper time delay, to obtain the ground motion from the entire fault. A new variation of this approach is introduced based on a "dynamic corner frequency." In this model, the corner frequency is a function of time, and the rupture history controls the frequency content of the simulated time series of each subfault. The rupture begins with a high corner frequency and progresses to lower corner frequencies as the ruptured area grows. Limiting the number of active subfaults in the calculation of dynamic corner frequency can control the amplitude of lower frequencies.

Our dynamic corner frequency approach has several advantages over previous formulations of the stochastic finite-fault method, including conservation of radiated energy at high frequencies regardless of subfault size, application to a broader magnitude range, and control of the relative amplitude of higher versus lower frequencies. The model parameters of the new approach are calibrated by finding the best overall fit to a ground-motion database from 27 well-recorded earthquakes in California. The lowest average residuals are obtained for a dynamic corner frequency model with a stress drop of 60 bars and with 25% of the fault actively slipping at any time in the rupture.

As an additional tool to allow the stochastic modeling to generate the impulsive long-period velocity pulses that can be caused by forward directivity of the source, the analytical approach proposed by Mavroeidis and Papageorgiou (2003) has been included in our program. This novel mathematical model of near-fault ground motions is based on a few additional input parameters that have an unambiguous physical meaning; the method has been shown by Mavroeidis and Papageorgiou to simulate the entire set of available near-fault displacement and velocity records, as well as the corresponding deformation, velocity, and acceleration response spectra. The inclusion of this analytical model of long-period pulses substantially increases the power of the stochastic finite-fault simulation method to model broadband time histories over a wide range of distances, magnitudes, and frequencies.

Introduction

The effects of a large earthquake source, including fault geometry, heterogeneity of slip on the fault plane, and directivity, can profoundly influence the amplitudes, frequency content, and duration of ground motion. Finite-fault modeling has therefore been an important tool for the prediction of ground motion near the epicenters of large earthquakes (Hartzell, 1978; Irikura, 1983; Joyner and Boore, 1986; Heaton and Hartzell, 1986; Somerville *et al.*, 1991; Tumarkin and Archuleta, 1994; Zeng *et al.*, 1994; Beresnev and Atkinson, 1998a). One of the most useful methods to simulate ground motion for a large earthquake is based on the simulation of several small earthquakes as subevents that comprise a large fault-rupture event. A large fault is divided into N subfaults and each subfault is considered as a small point source (introduced by Hartzell, 1978). The rupture spreads radially from the hypocenter. In our implementation, the ground motions of subfaults, each of which is calculated by the stochastic point-source method, are summed with a proper time delay in the time domain to obtain the ground-motion acceleration, $a(t)$, from the entire fault,

$$a(t) = \sum_{i=1}^{nl} \sum_{j=1}^{nw} a_{ij}(t + \Delta t_{ij}), \tag{1}$$

where nl and nw are the number of subfaults along the length and width of main fault, respectively ($nl \times nw = N$), and Δt_{ij} is the relative delay time for the radiated wave from the ijth subfault to reach the observation point. The $a_{ij}(t)$ are each calculated by the stochastic point-source method as described by Boore (1983) and summarized below.

The acceleration spectrum for a subfault at a distance R_{ij} maybe modeled as a point source with an ω^2 shape (Aki, 1967; Brune, 1970; Boore 1983). The acceleration spectrum of shear wave of the ijth subfault, $A_{ij}(f)$, is described by

$$A_{ij}(f) = \{CM_{0ij}(2\pi f)^2/[1 + (f_{0ij})^2]\}\{\exp(-\pi f\kappa)\exp(-\pi f R_{ij}/Q\beta)/R_{ij}\}, \quad (2)$$

where M_{0ij}, f_{0ij}, and R_{ij} are the ijth subfault seismic moment, corner frequency, and distance from the observation point, respectively. The constant $C = \Re^{\theta\varphi}FV/(4\pi\rho\beta^3)$, where $\Re^{\theta\varphi}$ is radiation pattern (average value of 0.55 for shear waves), F is free surface amplification (2.0), V is partition onto two horizontal components (0.71), ρ is density, and β is shear-wave velocity. Corner frequency, f_{0ij}, is given by $f_{0ij} = 4.9E + 6\,\beta(\Delta\sigma/M_{0ij})^{1/3}$, where $\Delta\sigma$ is stress drop in bars, M_{0ij} is in dyne cm and β is in kilometers per second (Boore, 1983). The term $\exp(-\pi f\kappa)$ is a high-cut filter to model near-surface "kappa" effects: this is the commonly observed rapid spectral decay at high frequencies (Anderson and Hough, 1984). The quality factor, $Q(f)$, is inversely related to anelastic attenuation. The implied $1/R$ geometric attenuation term is applicable for body-wave spreading in a whole space.

The approach of the stochastic point-source model is to generate a transient time series that has a stochastic character, and whose spectrum matches a specified desired amplitude spectrum such as that given by equation (2) (Boore, 1983). First, a window is applied to a time series of Gaussian noise with zero mean and unit variance. The windowed time series is transformed to the frequency domain and the amplitude spectrum of the random time series is multiplied by the desired spectrum as given by equation (2). Transformation back to the time domain results in a stochastic time series whose amplitude spectrum is the same as the desired spectrum on average. In extending this method to finite faults, we use equation (2) to describe the point-source Fourier spectrum of ground motion for each of the subfaults that make up the fault-rupture plane. The subfault spectra are Fourier transformed to the time domain, then summed at the observation point with the proper time delay (equation 1).

The moment of each subfault is controlled by the ratio of its area to the area of the main fault ($M_{0ij} = M_0/N$, where M_0 is the seismic moment of the entire fault). If the subfaults are not identical we can express the seismic moment of each subfault as follows:

$$M_{0ij} = \frac{M_0}{N}\,\frac{S_{ij}}{\sum_{l=1}^{nl}\left(\sum_{k=1}^{nw} S_{kl}/\right)/N}, \quad (3)$$

$$M_{0ij} = \frac{M_0 S_{ij}}{\sum_{l=1}^{nl}\sum_{k=1}^{nw} S_{kl}}, \quad (4)$$

where S_{ij} is the relative slip weight of the ijth subfault.

Studies have shown that in such kinematic models the obtained ground motion, $a(t)$, for a large fault depends on the subfault size or the number of subfaults, N (Joyner and Boore, 1986; Beresnev and Atkinson 1998b). In other words, to correctly reproduce observed ground motions for a large fault, there are some constraints on the subfault size or the number of subfaults. This constraint on subfault size in current stochastic finite-fault simulation methods is a conceptual drawback, because, intuitively, the simulated ground motions should be independent of the fault-discretization scheme. There are other significant drawbacks to current stochastic simulation schemes. They do not attempt to model the phasing of various arrivals in the signal at large distances, such as early body-wave arrivals followed by later surface-wave arrivals. At near-fault distances, stochastic methods have not adequately described the coherent long-period pulses that may control the period, duration, and amplitude of near-fault ground motions at periods longer than about 1 sec.

Use of Stochastic versus Deterministic Simulation Methods

Given the acknowledged limitations of stochastic methods at lower frequencies, a valid question may be: why use stochastic methods at all? Perhaps such methods should be abandoned in favor of deterministic methods or hybrid methods that use the stochastic approach only at high frequencies. This question warrants careful examination. It is widely recognized that near-fault ground motions may be strongly influenced by long-period pulses caused by forward rupture directivity of the source and that the resulting ground motions at long periods are well matched by deterministic simulation methods based on kinematic slip models (Pitarka *et al.*, 2000, 2002). On the other hand, deterministic methods produce synthetics that do not have the complexity at high frequencies that is present in the real Earth. Stochastic simulations are widely held to be the most successful at predicting ground motion at frequencies above 1 Hz, probably because of the importance of scattering effects at high frequencies (Hartzell *et al.*, 1999). It is natural, then, that hybrid methods have developed that combine the low-frequency advantages of deterministic methods with the high-frequency advantages of stochastic methods, thereby allowing broadband simulation of time histories (Hartzell *et al.*, 1999; Pitarka *et al.*, 2000, 2002). What all the simulation methods (deterministic, stochastic, and hybrid) have in common is that they rely on the summation of subevents or Green's functions, but they differ in the summation approaches and rules. There are also many possible variations on the subevent records to be used in the summation. They may be empirical Green's functions from small earthquakes, stochastic synthetics, or synthetics based on elastic wave propagation (see Hartzell *et al.* [1999] for a review of the possible combinations). Hybrid approaches are often cited as being the most versatile (Hartzell *et al.*, 1999; Pitarka *et al.*, 2000, 2002). The ground displacement at an observation point can be determined based on the slip distribution on the fault and the impulse response of the medium (Green's function), according to the discretized representation theorem (Aki and Richards, 1980). In hybrid methods, the low-frequency part of the Green's function is deterministic, based on elastic wave-propagation methods, whereas the high-frequency part is based on a stochastic Brune model (Hartzell *et al.*, 1999). Thus, the hybrid models cover a broad frequency range, from about 0.1 to 20 Hz. However, hybrid methods may not necessarily provide Green's functions that satisfy both the amplitude and phase information in the important intermediate frequency range from 0.5 to 2 Hz; the source processes generating the 0.5- to 2-Hz motions are not adequately resolved by either low- or high-frequency models (Miyake *et al.*, 2003).

In theory, hybrid methods should perform better than purely stochastic methods in predicting ground motions from earthquakes across a broad-frequency range. In practice, the situation appears less than clear-cut, partly because numerous modifications have been made to stochastic methods that allow them to mimic the salient features of earthquakes at longer periods. A comprehensive study of various simulation methods, and their ability to fit the near-fault motions of the 1994 Northridge, California, earthquake, was performed by Hartzell *et al.* (1999). They examined 13 combinations of simulation models from the purely stochastic to the purely deterministic, including two hybrid approaches. From the point of view of this study, the most relevant cases considered were the stochastic finite-fault simulations using the method of Beresnev and Atkinson (1998b), and the two hybrid approaches. The hybrid approaches make use of the actual slip distribution on the fault as determined by the ground-motion data. The stochastic simulations considered the cases of uniform or random slip distribution, with the random slip distribution being the most relevant case, in terms of ground-motion prediction. The first hybrid model used the laterally homogeneous, kinematic slip results at low frequencies, combined with stochastic results at high frequencies. The second hybrid approach combined the 3D finite-difference, kinematic results for the Northridge inversion slip distribution at low frequencies with the same high-frequency synthetics as the first hybrid model. Thus, both hybrid methods used considerable additional information over that used by the stochastic method and should have outperformed the stochastic method of Beresnev and Atkinson (1998b) for this hindcast exercise. Surprisingly, this was not the case. Plots of response spectra showed that both the finite-fault stochastic and hybrid methods performed equally well across a broad range of frequencies, from 0.1 to 20 Hz (Hartzell *et al.*, 1999). Looking at a table of time-domain comparisons of model bias, Hartzell *et al.* (1999) concluded that the hybrid methods were preferable overall. However, the statistics presented by Hartzell *et al.* (1999) could just as easily be interpreted to reach the opposite conclusion. In Table 1, we reproduce their comparison of model bias (defined as the ratio of the observed parameter to the simulated parameter, taken over all observations) for the Beresnev and Atkinson (1998b) stochastic finite-fault model (FINSIM), in comparison with the two hybrid models. The table shows the model bias for the peak velocity, peak acceleration, velocity duration, and acceleration duration (as measured from the time-domain traces for both the observed and simulated records). Based on their comparison, Hartzell *et al.* concluded that hybrid models match the time-domain characteristics of the ground motions better than the stochastic finite-fault model does. Referring to Table 1, the hybrid 2 method performs the best in matching durations. However, the hybrid 2 model underpredicts peak amplitudes. The stochastic model does the best job of predicting both peak acceleration and velocity, despite use of a random slip distribution, and does just as well as the hybrid 1 model in predicting the durations. Thus, it could be concluded from the information presented by Hartzell *et al.* that the stochastic model performs better than the hybrid model, with the possible exception of cases in which the 3D velocity structure is needed to more accurately model ground-motion characteristics in the time domain.

The stochastic method has a long history of performing better than it should in terms of matching observed ground-motion characteristics. It is a simple tool that combines a good deal of empiricism with a little seismology and yet has been as successful as more sophisticated methods in predicting ground-motion amplitudes over a broad range of magnitudes, distances, frequencies, and tectonic environments. It has the considerable advantage of being simple and versatile and requiring little advance information on the slip distribution or details of the Earth structure. For this reason, it is not only a good modeling tool for past earthquakes, but a valuable tool for predicting ground motion for future events with unknown slip distributions. It has been used in

Table 1
Model Bias for the Northridge Earthquake Based on Time-Domain Measures

Method	V_{max}	A_{max}	T_V	T_A
FINSIM	1.007	1.006	1.985	1.398
Hybrid 1	1.021	1.131	1.829	1.448
Hybrid 2	1.263	1.181	0.841	1.124

Results are given for (1) finite-fault stochastic simulations made with FINSIM (random slip distribution) and for (2) hybrid 1 method and (3) hybrid 2 method with 3D velocity model of the region, in addition to the Northridge slip distribution. Extracted from table 7 in Hartzell *et al.* (1999). Bias is given as a factor, for maximum velocity and acceleration, and duration of velocity and acceleration. All methods reproduce response spectra in the range from 0.1 to 20 Hz.

a wide variety of studies and tectonic environments, including California (Hanks and McGuire, 1981; Boore, 1983; Joyner, 1984; Joyner and Boore, 1988; Schneider *et al.*, 1993; Atkinson and Silva, 1997, 2000), eastern North America (Atkinson, 1984; Boore and Atkinson, 1987; Toro and McGuire, 1987; Ou and Herrmann, 1990; Atkinson and Boore, 1995; Toro *et al.*, 1997), Mexico (Beresnev and Atkinson, 1998a; Singh *et al.*, 1989), the Cascadia region (Silva *et al.*, 1991; Atkinson and Boore, 1997), Greece (Margaris and Boore, 1998), Russia (Sokolov, 1997), and Italy (Rovelli *et al.*, 1991, 1994; Berardi *et al.*, 1999). In our view, the history of success of the stochastic model is a good reason to continue to work on its development, improve its shortcomings, and broaden its utility. The stochastic method may also provide an additional avenue to explore the question of whether areas of concentrated slip, as resolved by deterministic methods, are directly related to the areas on the fault that generate strong ground motion, as proposed by Miyake *et al.* (2003). Users of ground-motion simulation methodologies should consider the potential advantages of a variety of methods and reach their own conclusions. In this article, we focus on further development of stochastic finite-fault methods and continue to explore the fertile territory that lies between purely stochastic and purely deterministic treatments of ground-motion generation. In particular, we address some conceptual disadvantages of current stochastic finite-fault approaches and introduce improvements to the treatment of low-frequency ground motions to allow better modeling of long-period velocity pulses.

The Dependence of Radiated Energy on Subfault Size

Subfault size dependence in stochastic finite-fault modeling, as demonstrated by Joyner and Boore (1986) and Beresnev and Atkinson (1998b), raises a question. Is the total radiated energy from the fault conserved when we change the subfault size or the number of subfaults? Let us free the simulations from the constraint of specified subfault size and study its consequences. The square of the Fourier spectrum is proportional to the received energy from each subfault. Let us consider a vertical fault with length of 40 km and width of 20 km. The approximate moment magnitude for such a fault, based on Wells and Coppersmith (1994), is **M** 7.0. Table 2 lists all the assumed input parameters that we use to model ground motions from such a fault (see Beresnev and Atkinson [2002] for details). We use the stochastic finite-fault simulation algorithm FINSIM (Beresnev and Atkinson, 1998a). We vary the number of subfaults into which the fault is divided and calculate the total received energy from the fault at the observation point. All the other parameters have been kept the same in all simulations. In this step all the subfaults are square and identical in slip behavior and corner frequency. The observation point is far from the fault surface (more than 300 km) so that the attenuation effect will be almost the same for all the subfaults. Simulations are performed for different subfault lengths, including 1, 2, 5, and 10 km. The number of subfaults is 800, 200, 32, and 8, respectively, covering a wide range of subfault sizes. The size of the main fault is the same for all cases.

Figure 1 shows the total received energy at the observation point for different subfault lengths. It shows that, as we increase the number of subfaults, the energy at low frequencies is decreased and the energy at high frequencies is increased. If the entire fault is considered as 800 subfaults with the size of 1 km by 1 km, the total received energy at

Table 2
Assumed Model Parameters for Simulation Exercises with FINSIM

$Q\ (f)$	$333f^{0.74}$
Distance-dependent duration	$T_0 + 0.1R$
Kappa	0.03
Crustal shear-wave velocity (km/sec)	3.7
Crustal density (g/cm^3)	2.8
Geometric spreading	$1/R$ ($R \leq 70$ km)
	$1/R^0$ (70 km $< R <$ 130 km)
	$1/R^{0.5}$ ($R \geq 130$ km)
Stress drop (bars)	50
Strength factor	1.6

These parameters are typical for finite-fault simulations (Beresnev and Atkinson, 2002).

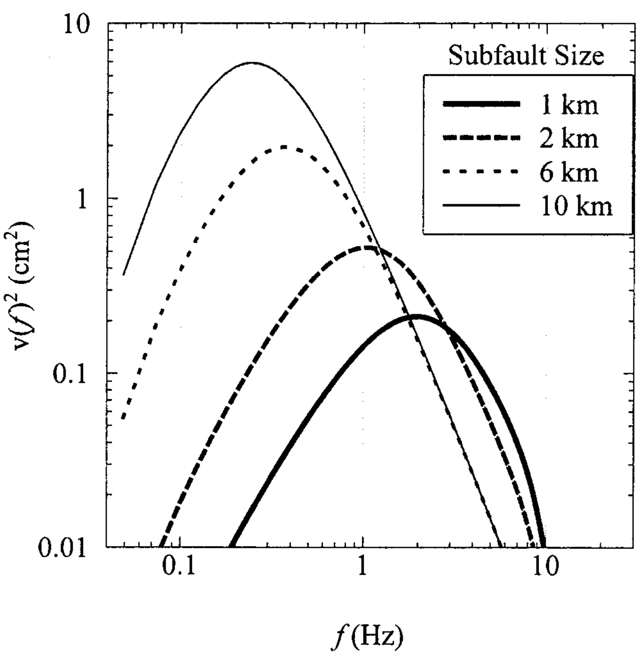

Figure 1. Far-field received energy of a fault with different subfault lengths by using the static corner frequency approach, for an event of **M** 7 at 333 km. If the entire fault is considered as 800 subfaults with the size of 1 km by 1 km, the total received energy at the observation point is much larger than the total received energy when the entire fault is considered as eight subfaults with the size of 10 km by 10 km.

the observation point is much larger than the total received energy is when the entire fault is considered as eight subfaults, each with the size of 10 km by 10 km. Because the attenuation effects are almost the same for all the subfaults in the far field, it follows that the total radiated energy from the entire fault is not conserved. This is a conceptual disadvantage that applies to the current popular stochastic finite-fault formulations.

Dynamic Corner Frequency

Different definitions are possible for the corner frequency of an earthquake spectrum. In the stochastic point-source approach the original definition of corner frequency was given by $f_0 = 4.9E + 6\beta(\Delta\sigma/M_0)^{1/3}$, where $\Delta\sigma$ is the stress drop in bars, M_0 is the seismic moment in dyne cm, and β is the shear-wave velocity in kilometers per second (Boore, 1983). This expression follows from the Brune (1970, 1971) point-source model. Other expressions that have been proposed, involving rupture duration T, are $f_{0ij} = 1/T$ (based on equation 6 in Boore [1983]), where T is rupture duration; $f_{0ij} = 0.5/T$ (based on Boatwright and Choy [1992]), where T is rupture duration; and $f_{0ij} = 0.37/T$ (Hough and Dreger, 1995, p. 1582), where $T = L/(2y\beta)$, in which L is the fault dimension and y is the ratio of rupture velocity to shear-wave velocity. Another definition suggests that corner frequency depends on the azimuth of rupture-propagation direction, $f_{0ij} = 1/T(1 - y \cos \theta)$, where θ is the rupture-propagation direction (Hirasawa and Stauder, 1965). In all these definitions, corner frequency is inversely proportional to the ruptured area or duration either explicitly or implicitly.

In finite-fault modeling, we deal with a ruptured area, $a_r(t)$, which is time dependent; it is initially zero and is finally equal to the entire fault area. If the rupture stops at the end of the first subfault, the corner frequency is inversely proportional to the area of the first subfault. If the rupture stops at the end of the ninth subfault, the corner frequency is inversely proportional to the ruptured area, which is the area of the nine subfaults. Eventually, when the rupture stops at the end of the Nth subfault, the corner frequency is inversely proportional to the entire ruptured area. Thus, if corner frequency is inversely proportional to the ruptured area, it follows that the corner frequency in finite-fault modeling can be considered as a function of time. Similarly, it also follows that corner frequency should be decreasing as the signal duration builds. Thus, at each moment of time the corner frequency depends on the cumulative ruptured area. The rupture begins with high corner frequencies and progresses to lower corner frequencies. Let us consider a dynamic definition of corner frequency and assess its consequences.

In our dynamic approach, the corner frequency of the first subfault (near the beginning of rupture) is $f_{011} = 4.9E + 6\beta(\Delta\sigma/M_{011})^{1/3}$, where M_{011} is the seismic moment of the first subfault. The dynamic corner frequency of the ijth subfault, $f_{0ij}(t)$, can be defined as a function of $N_R(t)$, the cumulative number of ruptured subfaults at time t:

$$f_{0ij}(t) = N_R(t)^{-1/3}\ 4.9E + 6\beta(\Delta\sigma/M_{0\mathrm{ave}})^{1/3}, \qquad (5)$$

where $M_{0\mathrm{ave}} = M_0/N$ is the average seismic moment of subfaults. For $t = t_{\mathrm{end}}$, the number of ruptured subfaults, $N_R(t)^{-1/3} = N^{-1/3}$. Thus, the corner frequency at the end of rupture is $f_{0ij}(t_{\mathrm{end}}) = N^{-1/3}\ 4.9E + 6\beta(\Delta\sigma/M_0/N)^{1/3}$, which leads us to $f_{0ij}(t_{\mathrm{end}}) = f_0$, which is the corner frequency of the entire fault. Thus, the lower limit of the dynamic corner frequency is the corner frequency of the entire fault.

As the rupture propagates toward the end of the fault, the number of ruptured subfaults increases; hence, the corner frequency of the subfaults and of the radiated spectrum decreases. The dynamic corner frequency concept will tend to decrease the level of the spectrum of the subfaults and hence their radiated energy at high frequencies as the corner frequency decreases ($A_{ij}(f)_{f \gg f0ij} \propto f_{0ij}{}^2$). We therefore introduce a scaling factor to balance this tendency and conserve the total radiated energy of subfaults at high frequencies. The high-frequency spectral level from each subfault should be the same if all subfaults are identical. Thus, we express the acceleration spectrum of the ijth subfault, $A_{ij}(f)$, as follows:

$$A_{ij}(f) = C\ M_{0ij}H_{ij}(2\pi f)^2/[1 + (f/f_{0ij})^2], \qquad (6)$$

where H_{ij} is a scaling factor that we will apply to conserve the high-frequency spectral level of subfaults. Note that this will result in an overall conservation of energy, because most of the energy in the spectrum comes from the area above the corner frequency. The total radiated energy at high frequencies from the entire fault (E) should be N times greater than the radiated energy at high frequencies from the ijth subfault (E_{ij}). Therefore,

$$\begin{aligned} E_{ij} &= E/N, \\ E_{ij} &= (1/N)\int\{CM_0(2\pi f)^2/[1 + (f/f_0)^2]\}df. \end{aligned} \qquad (7)$$

On the other hand, based on equation (6), the radiated energy at high frequencies from the ijth subfault should be

$$E_{ij} = \int\{CM_{0ij}H_{ij}(2\pi f)^2/[1 + (f/f_0)^2]\}df. \qquad (8)$$

Considering $M_{0ij} = M_0/N$, we can find H_{ij}, the scaling factor, by equating equations (7) and (8):

$$H_{ij} = \left(N\int\{f^2/[1 + (f/f_0)^2]\}df \Big/ \int\{f^2/[1 + (f/f_{0ij})^2]\}df\right)^{1/2}. \qquad (9)$$

Because we deal with discrete data in the frequency domain, equation (9) can be rewritten as follows:

$$H_{ij} = \left(N\Sigma\{f^2/[1 + (f/f_0)^2]\}/\Sigma\{f^2/[1 + (f/f_{0ij})^2]\}\right)^{1/2}. \quad (10)$$

Equation (10) can be calculated numerically in the frequency domain to obtain H_{ij} for each subfault. The total radiated energy from the *ij*th subfault is then equal to the total radiated energy from the first subfault, but the calculation of corner frequency, which controls the shape of the spectrum, comes from the total ruptured area. Thus, the total radiated energy of subfaults does not change as the rupture propagates, but the distribution of energy tends to shift toward lower frequencies.

The dynamic corner frequency was applied to the simulation cases discussed previously (Fig. 1). The simulations were performed by modifying the FINSIM code of Beresnev and Atkinson (1998a) to implement the dynamic corner frequency definition as given in equation (5), with the subfault acceleration spectrum as given by equation (6). The modified code has been named EXSIM to avoid confusion. Table 3 shows the input parameters to EXSIM. Figure 2 shows the impact of the new formulation in terms of energy. Comparison of Figure 2 with Figure 1 shows an important advantage of the dynamic corner frequency approach. In Figure 2, we see that the total radiated energy from the fault is almost identical for all cases, whereas in the "static corner frequency" approach (Fig. 1) the radiated energy depends on subfault size. Because the total radiated energy is the same over a wide range of subfault sizes, we can now apply an arbitrary constant subfault size, say 1 km by 1 km, for simulations using the dynamic corner frequency approach. The ability to free the simulation from constraints on subfault size allows a wider magnitude range of application, as we will show later.

Because the factor H_{ij} scales the spectrum at all frequencies, the spectrum of the simulated time series at low frequencies may not converge exactly to the level that is representative of the seismic moment. Figure 3 illustrates the behavior of the displacement spectra of the simulated time series at low frequencies, comparing the spectra for various subfault sizes with those predicted by a Brune point-source model for the given moment and distance. Figure 3 shows that the influence of the scaling factor on the displacement spectra at low frequencies is typically small, representing less than 0.1 magnitude units. Furthermore, the energy associated with lower frequencies is very low compared with the amount of energy associated with higher frequencies.

To scale the amplitude of lower frequencies to the level that is representative of the seismic moment of each subfault, we may taper the value of H_{ij} such that it gradually approaches unity at low frequencies (below the corner frequency of the main fault). The practical effect of this taper function on the time series and response spectra in the frequency range of engineering interest is negligible. Thus, the seismic moment is conserved overall through the assignment of moment to each subfault (equation 4), whereas the diminishing effect of dynamic corner frequency on high-frequency spectral amplitude is compensated for by the scaling factor, H, such that the total area under the spectrum is conserved.

Table 3
Modeling Parameters for Simulation Exercises with EXSIM

Q (f)	$333f^{0.74}$
Distance-dependent duration	$T_0 + 0.1R$
Kappa	0.03
Crustal shear-wave velocity (km/sec)	3.7
Crustal density (g/cm^3)	2.8
Geometric spreading	$1/R$ ($R \leq 70$ km)
	$1/R^0$ (70 km $< R <$ 130 km)
	$1/R^{0.5}$ ($R \geq 130$ km)
Stress drop (bars)	50
Pulsing area percentage	50%

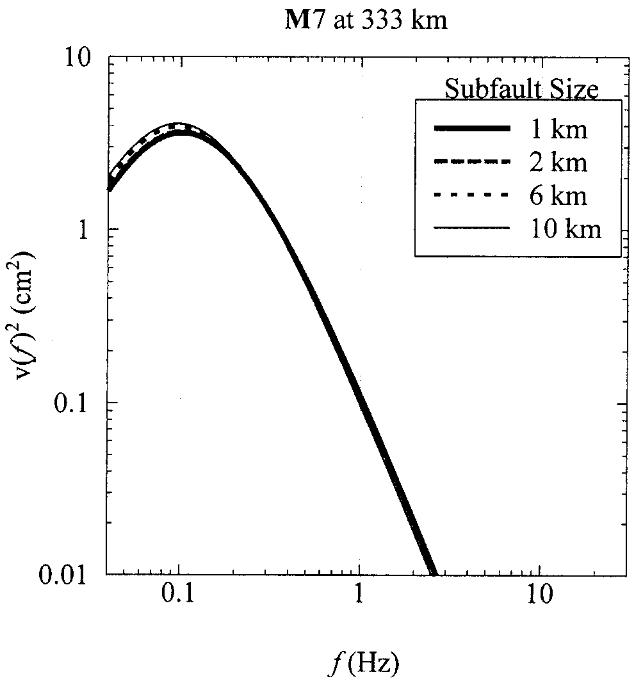

Figure 2. Far-field received energy of a fault with different subfault lengths by using the dynamic corner frequency approach, for an event of **M** 7 at 333 km. Total radiated energy from the fault is almost identical for all cases. (Note, the paths from the subfaults to the observation point are not exactly the same, and therefore the attenuation effects are not identical for all the subfaults. This explains the small differences between total received energy observed for different subfault-size cases.)

Pulsing Subfaults

In actual earthquake ruptures, the slip may only be occurring on part of the fault at any one time. Heaton (1990) proposed the concept of a "self-healing" model, in which the duration of slip at any location on the fault is short. For example, inversion of the Northridge earthquake data by Wald *et al.* (1996) suggests that slip duration is less than 1.5 sec, whereas the rupture propagation duration was about 7 sec. In stochastic modeling, we can consider a form of this behavior, in which only part of the fault is actively pulsing at any time. In such a model, the areas that are actively pulsing contribute to the ground-motion radiation, but the other areas on the fault are passive. The passive cells will have no effect on the dynamic corner frequency. The active area will move along the fault as rupture progresses.

In our implementation of this concept in EXSIM, the cumulative number of pulsing subfaults, as given by N_R in equation (5), increases with time at the beginning of rupture but becomes constant after a while, at some fixed percentage of the total rupture area. Thus, the dynamic corner frequency decreases with time near the beginning of the rupture and then becomes constant. The behavior is controlled through a parameter that gives the maximum active pulsing area. A pulsing area of 50% means that during the rupture of a subfault, at most, 50% of all the subfaults are active and thus contributing to the dynamic corner frequency. The remaining subfaults are passive.

Although this concept is inspired by the self-healing model of Heaton (1990), we caution that it is significantly different in some respects. In the self-healing model, the pulse duration will not increase with time at the beginning of the rupture, and it may be very short in relation to the overall rupture duration. Thus, we do not attribute to our concept of an active pulsing area any direct physical connection with the self-healing slip pulse. Nevertheless, the option to have only a part of the rupture actively participate in the slip at any time does acknowledge the reality that slip near the beginning of a large rupture may have stopped by the time the rupture-propagation front finally reaches the end of the fault. This may result in more realistic modeling of ground-motion generation from a finite fault.

The total received energy will decrease as the percentage of pulsing area decreases, but the ground motions remain independent of the size of the subfaults. Figure 4 shows the effect of the percentage pulsing area on the response spectra at 100 km for our example **M** 7 fault (all for the input parameters of Table 3). The response spectrum for a stochastic point-source model is also shown, as calculated by using Boore's (1996) stochastic point-source algorithm SMSIM. By decreasing the pulsing area, the amplitudes at low frequencies decrease; thus, a narrow pulsing area on the fault results in lower amplitudes at longer periods and lower energy radiation. Variation of this parameter can be used to adjust the relative amplitudes of low-frequency motion in finite-fault modeling. Note that the pulsing length cannot be less than the length of one subfault.

High-frequency spectral amplitudes and high-frequency energy content are controlled by the stress drop (equations 2 and 5). Figure 5 shows response spectra for our **M** 7 example at 100 km for different stress drops. Thus, by varying

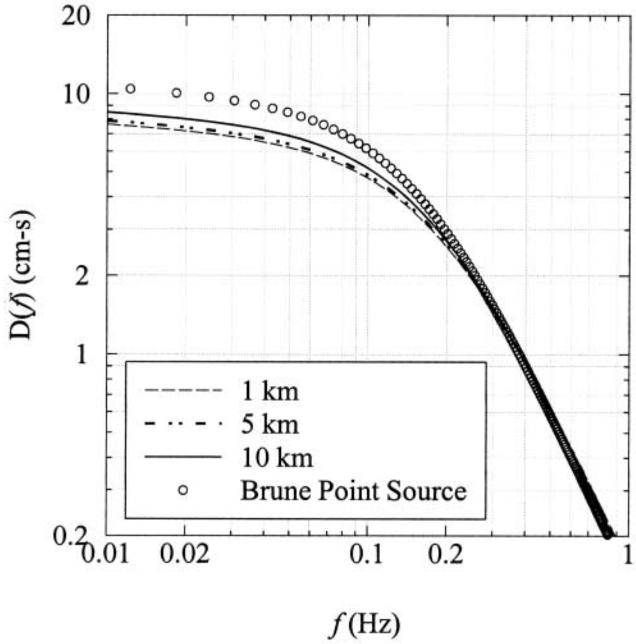

Figure 3. Fourier spectra of displacement, for an event of **M** 7 at 333 km, for different subfault lengths. The Brune point-source spectrum for this case is also shown (circles).

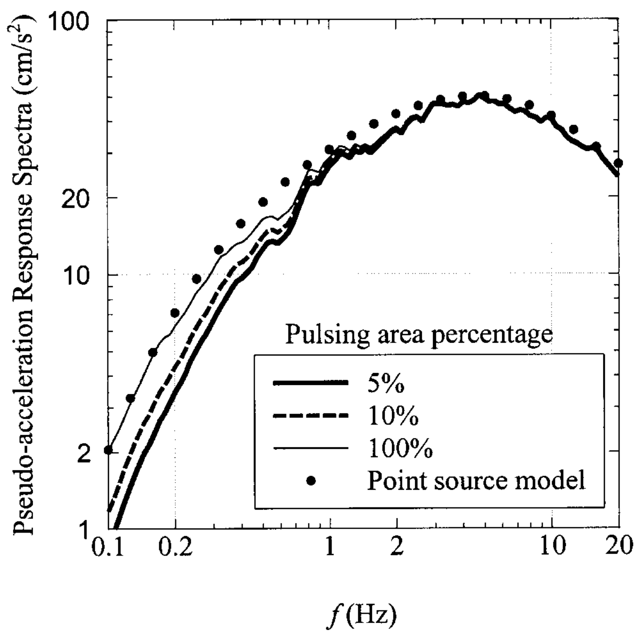

Figure 4. The 5% damped pseudoacceleration (PSA) response spectra for event of **M** 7 at $R = 100$ km for different pulsing area percentages by using the dynamic corner frequency finite-fault model (lines) and corresponding point-source model (circles). Assumed stress drop = 100 bars.

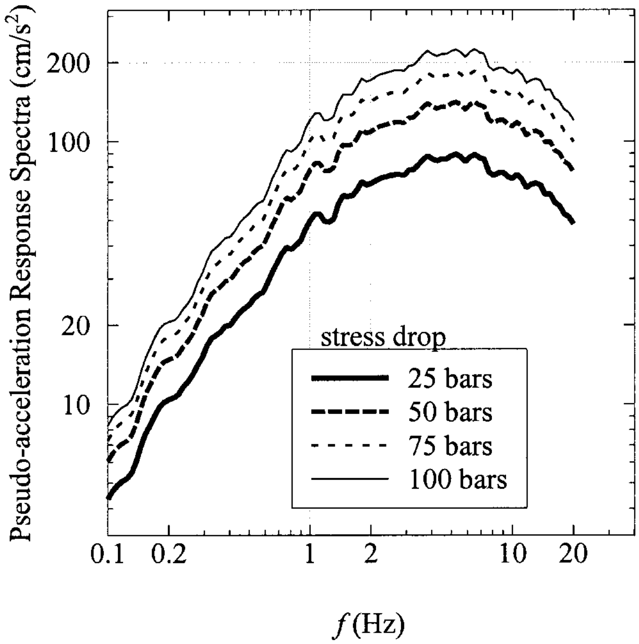

Figure 5. The 5% damped pseudoacceleration response spectra for event of **M** 7 at R = 100 km (25% pulsing area) for different stress parameters by using dynamic corner frequency. Assumed pulsing percentage = 25%.

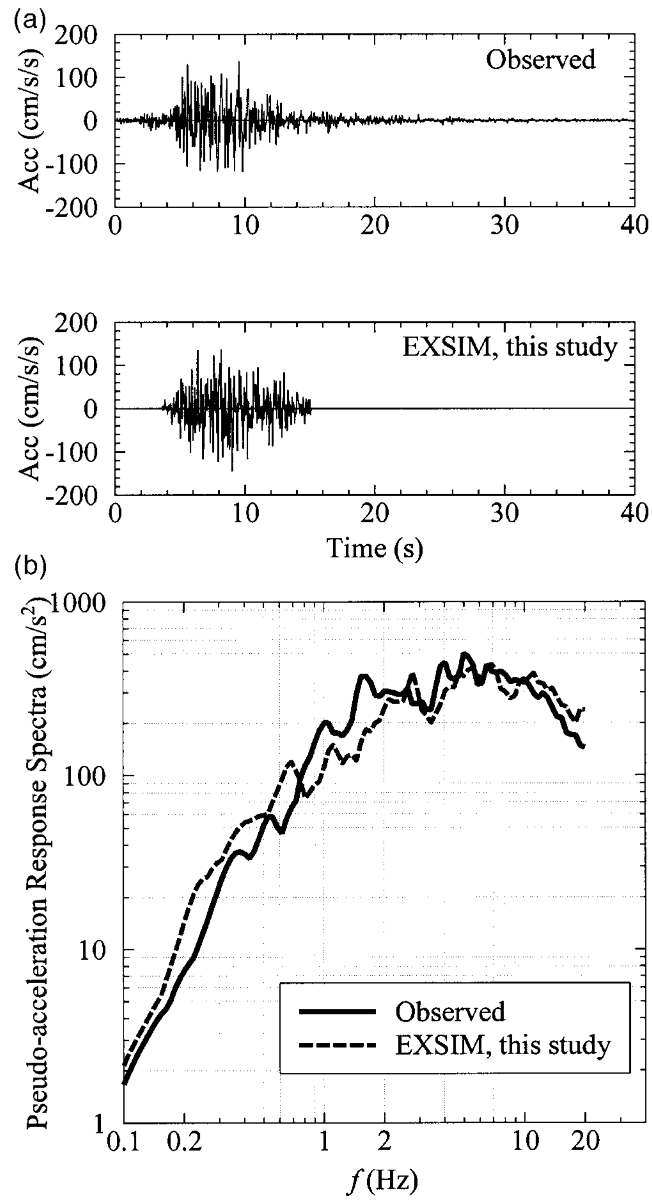

Figure 6. Simulated and observed horizontal components for **M** 6.7, 1994 Northridge earthquake at Vasquez Rocks Park station. (a) Time series; (b) 5% damped pseudoacceleration (Acc.) response spectra.

the percentage of pulsing area and stress drop, we can model different relative strengths of low- and high-frequency amplitudes.

Figure 6a shows a typical simulated time series for the Vasquez Rocks Park station, at a distance of 25 km from the **M** 6.7, 1994 Northridge fault rupture. A 20 km by 25 km fault plane with 122° E strike and 40° dip angle (toward the southeast) with the Northridge hypocenter was assumed by using the fault geometry of Wald *et al.* (1996). A satisfactory acceleration time series is obtained with a stress drop approximately equal to 60 bars and 25% pulsing area. The response spectra also match closely, as shown in Figure 6b. In future studies, the capability of the new model to characterize ground motions from specific events will be explored in more detail.

Preliminary Calibration of Model Parameters

There are two main "free" input parameters to our dynamic corner frequency finite-fault model: (1) stress drop controls the level of spectra at high frequencies, and (2) pulsing area percentage controls the level of spectra at low frequencies. To test our model and calibrate these model parameters for general applications, we used data from 27 moderate to large well-recorded earthquakes in California recorded on rock or stiff-soil sites (NEHRP C site class), as listed in Table 4. All observed data were obtained from the response-spectra database compiled by Pacific Engineering and Analysis (courtesy of W. J. Silva) as described in Atkinson and Silva (1997).

Our aim and scope in this exercise is to provide a general calibration of the model parameters for future events of unknown geometry, rather than to model individual events in detail. Therefore, we do not attempt to model the specifics of the rupture geometry and propagation for each of the events (some of which have well-known geometry, whereas others do not). Rather, for each event the fault size is assigned based on the empirical relationship between fault size and moment magnitude developed by Wells and Coppersmith (1994). Five random locations of the hypocenter on

Table 4
Calibration Events That Have Records on NEHRP C Site Conditions

Date			Event Name	Moment Magnitude	No. of records (C sites)	Station Distances (km)
yyyy	mm	dd				
1935	10	31	Helena	6.2	2	8
1952	11	22	Southern California	6.0	2	71
1957	3	22	San Francisco	5.3	2	10
1966	6	28	Parkfield	6.1	8	9, 10, 15, 60
1968	4	9	Borrego Mountain	6.8	2	126
1970	9	12	Lytle Creek	5.4	14	16, 20, 22, 23, 33, 46, 107
1971	2	9	San Fernando	6.6	46	3, 19, 20, 23, 24, 25, 27, 28, 29, 39, 58, 60, 65, 66, 68, 87, 112, 115, 123, 224
1974	11	28	Hollister	5.2	2	12
1975	6	7	Northern California	5.2	6	29, 59, 60
1975	8	1	Oroville	6.0	2	10
1975	8	2	Oroville	4.4	2	11
1975	8	8	Oroville aftershock	4.7	8	7, 9, 11
1978	8	13	Santa Barbara	6.0	2	36
1979	8	6	Coyote Lake	5.7	6	3, 9
1979	10	15	Imperial Valley	6.5	4	26
1980	1	24	Livermore	5.8	10	13, 18, 22, 30, 31
1980	1	27	Livermore	5.4	14	4, 8, 13, 18, 22, 30, 31
1980	2	25	Anza	4.9	6	6, 13, 41
1980	5	25	Mammoth Lake	6.3	2	16
1980	5	25	Mammoth Lake	5.7	2	25
1980	5	25	Mammoth Lake	6.0	6	20
1980	5	25	Mammoth Lake	5.7	6	15
1980	5	26	Mammoth Lake	6.1	2	17
1980	5	27	Mammoth Lake	6.0	4	20, 44
1980	5	27	Mammoth Lake	4.9	2	9
1980	5	31	Mammoth Lake	4.9	6	7, 9
1980	6	9	Victoria	6.1	2	35
1980	6	11	Mammoth Lakes aftershock	5.0	8	8, 9, 11, 12
1981	4	26	West Morland	5.8	2	26
1983	5	2	Coalinga	6.4	38	25, 28, 30, 32, 33, 35, 36, 37, 38, 39, 41, 44
1983	5	9	Coalinga	5.0	24	12, 13, 14, 20
1983	6	11	Coalinga	5.3	2	10
1983	7	9	Coalinga	5.2	18	10, 11, 12, 13, 14, 17
1983	7	22	Coalinga	5.8	14	8, 9, 10, 11, 12
1983	7	22	Coalinga	4.9	2	14
1983	7	25	Coalinga	5.2	2	15
1983	9	9	Coalinga	5.3	2	18
1986	7	20	Chalfant Valley	5.9	4	18, 26
1986	7	21	Chalfant Valley mainshock	6.2	12	23, 33, 36, 41, 51
1986	7	21	Chalfant Valley	5.6	2	14
1987	10	1	Whittier Narrows	6.0	52	11, 12, 21, 23, 25, 27, 29, 30, 33, 35, 38, 39, 43, 46, 53, 56, 60, 65, 71, 78
1987	10	4	Whittier Narrows	5.3	4	20, 43
1992	4	25	Cape Mendocino	7.1	4	9, 34
1992	6	28	Landers	7.3	28	1, 43, 51, 69, 96, 126, 132, 151, 163, 174, 194
1994	1	17	Northridge	6.7	36	8, 17, 22, 24, 27, 32, 35, 36, 37, 44, 45, 47, 71, 79, 85

the fault plane are considered, with a subroutine to choose a random i (between 1 and nl) and a random j (between 1 and nw) and then assigning the hypocenter to the ijth subfault. A random slip distribution is assumed by using a random number as the basis to assign a relative slip to each subfault. For each earthquake record, the moment magnitude and closest distance between the station and the fault are known. For this magnitude and distance, we simulate records for 15 values of azimuth from zero to 180 degrees, for each of the five hypocenters (a total of 75 simulated records for each recorded time series). We performed simulations for the 540 horizontal-component records in the California database that are classified as NEHRP C site class; these are soft-rock sites for which site amplification effects are not large.

(Note: the amplification for NEHRP C sites is assumed to be as given in Boore and Joyner [1997].) Table 5 shows the generic input parameters to EXSIM for all the simulations. All model parameters, except for the calibration parameters of stress drop and pulsing area, are as described by Beresnev and Atkinson (2002).

To calibrate the model parameters, we performed the simulations for a wide range of values of stress drop and pulsing area percentage to allow a grid search of the model error space (for more details see Motazedian [2004]). We calculated residuals for each record at each frequency, where the residual is defined as log(observed Pseudoacceleration [PSA]) − log(predicted PSA), where PSA is the horizontal-component of 5% damped pseudoacceleration. The lowest residuals averaged over all events and all frequencies from 0.14 Hz to 13 Hz are obtained for a stress drop of 60 bars with a 25% pulsing area. Figure 7 shows the average of the residuals versus frequency for the case of 60 bars stress drop and 25% pulsing area. The average residual is close to zero at all frequencies with the standard deviation (representing scatter of observations about the mean) ranging from 0.32 to 0.38 log units. Plots of the residuals versus magnitude and distance (not shown) indicate no obvious distance-dependent or magnitude-dependent trends in the obtained residuals. The small positive residual at low frequencies may be attributable to the contributions of long-period surface-wave generation by conversion of body waves at the boundary of deep sedimentary basins in California, which would influence some of the included records (Hanks, 1975; Lui and Heaton, 1984; Vidale and Helmberger, 1988; Campbell, 1997; Joyner, 2000). The presence of long-period coherent velocity pulses in some records, as discussed later, may also be a factor in the average low-frequency residual. We conclude that the dynamic corner frequency model, with stress drop of 60 bars and 25% pulsing area, reproduces average ground motions from California events of **M** 5 to **M** 7, over frequencies from 0.14 to 13 Hz. The relatively large standard deviation of residuals could be reduced by more detailed modeling of fault geometry and the characteristics of each individual event. These event-specific simulations will be the subject of future development. Our focus here has been to introduce the new concept of dynamic corner frequency and demonstrate its general applicability to simulation over a wide range of magnitude and distance. In addition, EXSIM has been successfully applied to simulate acceleration time series for **M** 3.0 to **M** 8.0 earthquakes in the development of ground-motion relations for Puerto Rico (D. Motazedian and G. Atkinson, unpublished manuscript, 2005).

Table 5

EXSIM Modeling Parameters for the Calibration of EXSIM, for California Earthquakes on NEHRP C Sites

$Q(f)$	$187f^{0.56}$
Distance-dependent duration	$T_0 + 0.1R$ (km)
Kappa	0.03
Crustal shear-wave velocity (km/sec)	3.7
Crustal density (g/cm^3)	2.8
Crustal amplification model	Boore and Joyner, 1997 (for California NEHRP C site conditions)
Geometric spreading	$1/R$ ($R \leq 40$ km) $1/R^{0.5}$ ($R > 40$ km)
Stress drop (bars)	60
Pulsing area percentage	25%

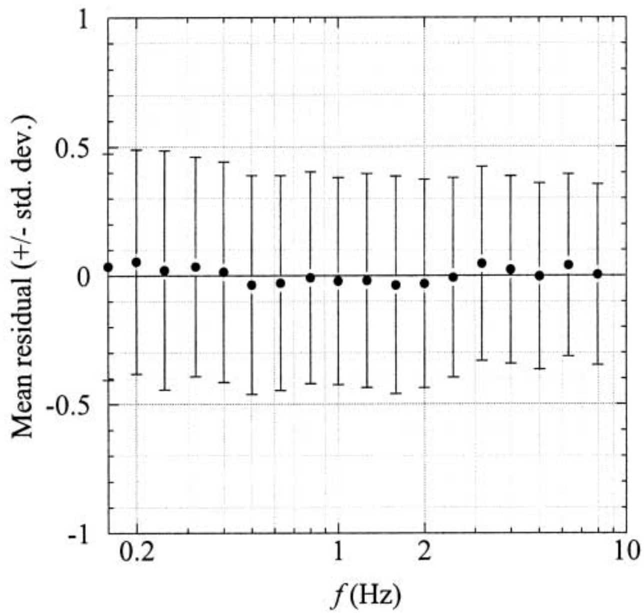

Figure 7. Average of residuals over all simulated California records (NEHRP C sites) versus frequency, where residual = log(observed PSA) − log(predicted PSA). Standard deviations of residuals are shown by error bars.

Comparison of Finite-Fault Simulations (EXSIM) with Stochastic Point-source Simulations (SMSIM) and Empirical Ground-Motion Relations

Let us compare the 5%-damped horizontal-component PSA at a range of distances for magnitudes **M** 5.5 and **M** 7.5 as generated by the EXSIM finite-fault approach with those generated by the stochastic point-source code SMSIM (Boore, 1996), and with empirical ground-motion relations for California. The input parameters describing the physical properties of the medium and the geometric and anelastic attenuation and duration are the same for both SMSIM and EXSIM (Table 5); a constant stress drop of 60 bars is assumed. In SMSIM, R is the distance of the observation point from the point source. In EXSIM, R is the closest distance to the fault plane. To cover a range of directivity effects in EXSIM, we simulated acceleration time series for a profile of stations distributed evenly around the fault plane at azimuths ranging from 0 to 360 degrees. For each magnitude, we simulated several events with randomly located hypocenters and random slip distributions. Figure 8 plots the results from SMSIM and EXSIM and compares them with the

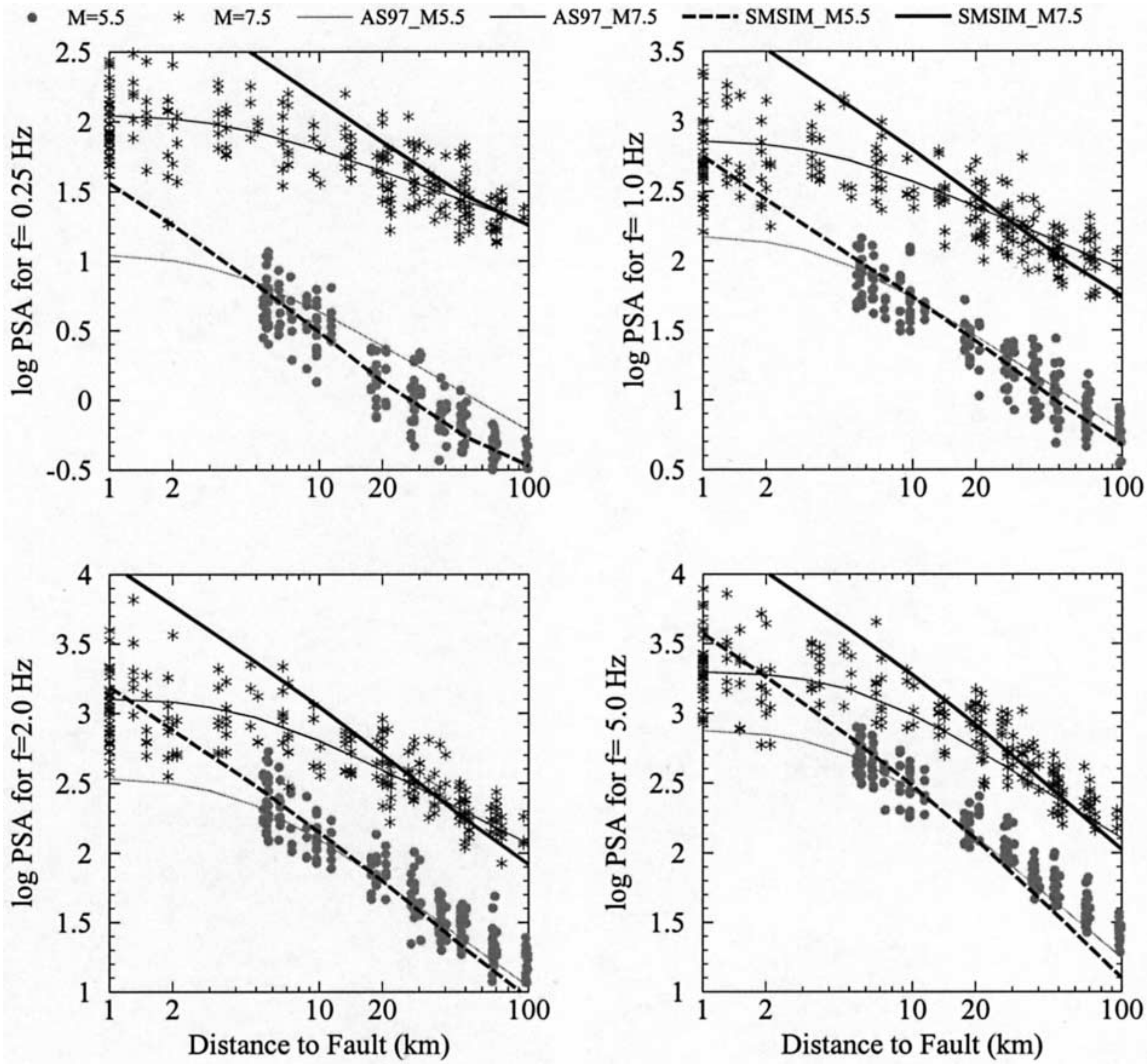

Figure 8. Comparison of PSA attenuation for **M** 5.5 and **M** 7.5 events in California from EXSIM model (symbols), SMSIM point-source (dotted lines), and empirical relations of Abrahamson and Silva (1997), all for NEHRP C sites, for frequencies of 0.25, 1, 2, and 5Hz.

predictions of empirical ground-motion relations for California (Abrahamson and Silva, 1997). Our finite-fault simulation results, using the calibrated stress drop of 60 bars and 25% pulsing area percentage, are consistent with the empirical ground-motion relations of Abrahamson and Silva (1997). The point-source model is consistent with the empirical ground-motion relations at distances greater than 20 km, but for large events it will overestimate the ground motion as we get close to the fault. (Note, this trend in the point-source model can be alleviated if a magnitude-dependent term is used to modify the distance at which the point source is located.) This distance trend is in agreement with the conclusions of Atkinson and Silva (1997, 2000). Furthermore, Beresnev and Atkinson (2002) show that there is an apparent decrease in the best-fit stress drop with increasing magnitude in point-source model applications. By contrast, when our finite-fault model is used, we match the empirical observations with a constant stress-drop model. Thus magnitude- and distance-dependent trends in point-source modeling appear to be artifacts introduced by the inappropriate modeling of an extended fault with a point source.

Mathematical Model of Near-fault Ground Motions (Mavroeidis and Papageorgiou Approach)

During past earthquakes, it has been observed that some near-fault stations have recorded velocity time series with a strong impulsive behavior (i.e., 2003, Bam, Iran; 1992, Landers, California, station LUC; 1966 Parkfield, California, station C02; 1971 San Fernando, California, PCD station; 1999 Chi-Chi, Taiwan, stations TCU068 and TCU052). A coherent long-period pulse is generated by forward directivity of the source and permanent translation effects (Mavroeidis and Papageorgiou, 2002). This long-period behavior has important engineering implications for flexible structures. Several studies have aimed to characterize the phenomenon (Campillo *et al.*, 1989; Abrahamson and Somerville, 1997; Somerville *et al.*, 1997; Papageorgiou, 1998; Somerville, 1998, 2000; Mavroeidis and Papageorgiou, 2002, 2003). Mavroeidis and Papageorgiou (2003) have introduced a novel mathematical model that can be used to include this impulsive behavior in stochastic and other modeling techniques. Their approach is rooted in an empirical description of the characteristics of near-fault strong ground motions. Their database comprises 165 records from within 20 km of different fault types, with earthquake magnitudes from 5.6 to 8.1, compiled from extensively studied events from all over the world. Mavroeidis and Papageorgiou show that the key parameters that define the waveform characteristics of near-fault velocity pulses are the pulse duration (or period), the pulse amplitude, and the number and phase of half-cycles. They define an analytical model that describes the near-fault velocity pulse in terms of these four parameters, as determined from the empirical data.

The pulse duration is defined as the inverse of the prevailing frequency of the signal: $T_p = 1/f_p$. The analytical expression for the ground-motion acceleration time histories, $a(t)$, is given by (Mavroedis and Papageorgiou, 2003):

$$a(t) = \begin{cases} -\dfrac{A\pi f_p}{\gamma}\left[\begin{array}{l}\sin\left(\dfrac{2\pi f_p}{\gamma}(t - t_0)\right)\cos[t\pi f_p(t - t_0) + v] \\ + \gamma\sin[2\pi f_p(t - t_0) + v]\left[1 + \cos\left(\dfrac{2\pi f_p}{\gamma}(t - t_0)\right)\right]\end{array}\right], & t_0 - \dfrac{\gamma}{2f_p} \le t \le t_0 + \dfrac{\gamma}{2f_p} \quad \text{with} \quad \gamma > 1 \\ 0, \text{ otherwise}, \end{cases} \tag{11}$$

where A, f_p, v, γ, and t_0 describe the signal amplitude, prevailing frequency, phase angle, oscillatory character, and time shift to specify the epoch of the envelope's peak, respectively. The parameter A is determined such that the amplitude of the synthetic waveform and its spectral peak agrees well with the corresponding quantities of the observed time series. The parameter $f_p = 1/T_p$, where T_p is pulse duration ($\log T_p = -2.2 + 0.4\,\mathbf{M}$). v and γ are adjusted to optimize the fitting of the synthetic records (see Mavroeidis and Papageorgious [2003] for more details). The methodology to include the analytical model of equation (11) in stochastic finite-fault modeling consists of many steps (Mavroeidis and Papageorgiou, 2003):

1. Apply equation (11) to generate an acceleration time series for a specific moment magnitude, for selected values of the model parameters.
2. Apply stochastic finite-fault modeling to generate acceleration time series for the same moment magnitude (in our case, the results of EXSIM).
3. Transfer both the analytical and stochastic acceleration time series to the frequency domain.
4. Subtract the Fourier amplitude spectrum of the time series generated in step 1 from the Fourier amplitude spectrum generated in step 2.
5. Return to the time domain, using the spectral amplitude from step 4 and the phase spectrum of the stochastic finite fault modeling from step 2.
6. Superimpose the time series generated in step 1 and step 5. The near-source pulse is shifted in time such that the peak of its envelope coincides with the time that the rupture front passes in front of the observation point.

An important advantage of the Mavroeidis and Papageorgiou (2003) model is that it has a sound empirical basis and has already been well calibrated in a generic sense for many earthquakes that have shown an impulsive long-period behavior. This behavior is not observed in all near-fault records, and thus the application of this model is not necessarily indicated for all cases.

We have programmed Mavroeidis and Papageorgiou's near-fault analytical model as an option in EXSIM. Thus, EXSIM can include stochastic and a combination of analytical and stochastic approaches in finite-fault modeling. Of course, the use of the analytical near-fault model requires the specification of additional parameters. In this article, we are not providing any new calibration beyond that provided by Mavroeidis and Papageorgiou, although we intend to investigate application of this methodology in more detail in future work. As an example, we have simulated the 1992 Landers earthquake at station LUC, based on the combined stochastic and analytical approach. This is a good record with which to illustrate the use of this model, because it features a very distinct low-frequency pulse that is difficult to model with traditional techniques. This can be seen clearly in the frequency domain in Figure 9. The stochastic model cannot reproduce this feature by using either a static (e.g., FINSIM) or dynamic corner frequency approach, but the combination of the stochastic and the analytical near-fault model reproduces the spectral content of the record well. In the analytical approach, the input parameters v, γ, and t_0 are 0.7, 50.0, and 4, respectively. T_p is pulse duration and is calculated by $\log T_\mathrm{p} = -2.2 + 0.4\,\mathbf{M}$. The input parameters for the dynamic corner frequency approach are the ge-

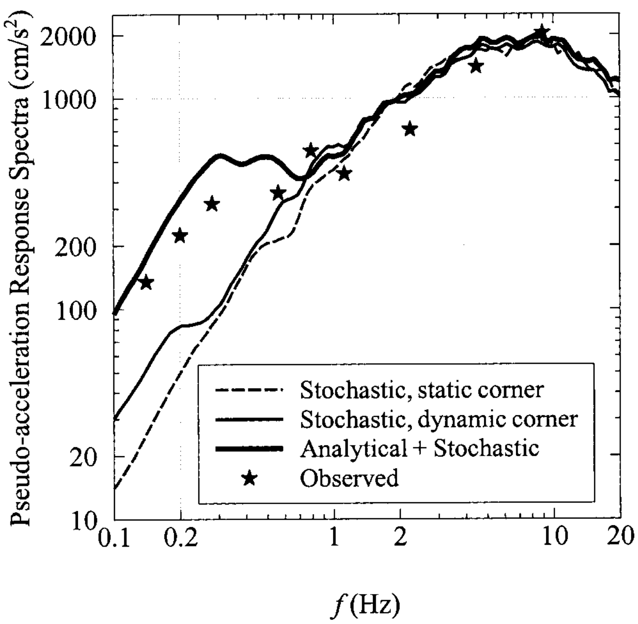

Figure 9. The 5% damped pseudoacceleration for **M** 7.2, 1992 Landers earthquake (station LUC), for the recorded (stars) and simulated (lines) waveforms. The combination of the analytical and stochastic approach best reproduces the large amplitudes observed at low frequencies.

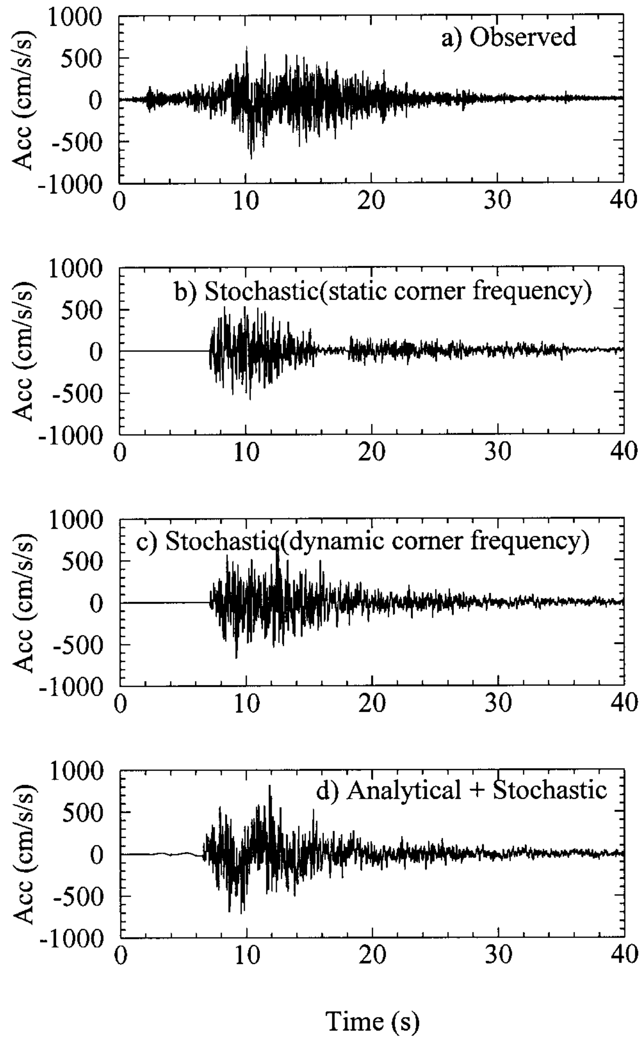

Figure 10. Recorded and simulated acceleration time series for **M** 7.2, 1992 Landers earthquake (station LUC). The simulated times series are based on static and dynamic corner frequency approaches and a combination of the analytical and stochastic approach.

neric parameters for California (Table 4), but with a pulsing area of 100% to maximize the spectral amplitudes at lower frequencies. The parameters of the static corner frequency approach have been adjusted to produce the same spectral amplitude at high frequencies as the dynamic corner frequency approach.

Figure 10 shows the recorded and simulated acceleration time series at LUC for the Landers earthquake, whereas Figure 11 shows the corresponding velocity traces. The gap in the static corner frequency simulation near 16 sec is an artifact caused by the fixed subfault size. This is improved in the simulation using the dynamic corner frequency approach, because a smaller subfault size is chosen to eliminate any such artifacts. However, neither the static nor dynamic corner frequency models match the long-period pulse that is apparent in both the acceleration and velocity traces. The combination of the stochastic and analytical model matches the characteristics of the LUC record well. We conclude that inclusion of the analytical near-fault model of Mavroeidis and Papageorgiou (2003) in EXSIM greatly enhances its ability to model impulsive near-fault ground motions that may dominate the signal at long periods in some cases. In addition, this hybrid modeling has also successfully simulated the observed impulsive behavior of the near-source records of the **M** 6.5 Bam (Iran) earthquake of 26 December 2003 (D. Motazedian and A. A. Moinfar, unpublished manuscript, 2004).

Discussion and Conclusions

The modifications to the stochastic finite-fault method proposed in this article include: (1) a new definition of corner frequency as a dynamic parameter that changes the frequency content of the ground motion as rupture progresses; (2) ability to consider a percentage of the fault as actively pulsing at any one time; (3) inclusion of the mathematical model of near-fault ground motions by Mavroeidis and Papageorgiou (2003) to allow extension of the stochastic method to modeling of impulsive long-period motions. We have shown that the modified model, based on the dynamic corner frequency, successfully reproduces the ground motions from a broad suite of earthquakes in California of **M** 5.0 to 7.3, using an assumed average stress drop of 60 bars and 25% active pulsing area. For specific near-fault records,

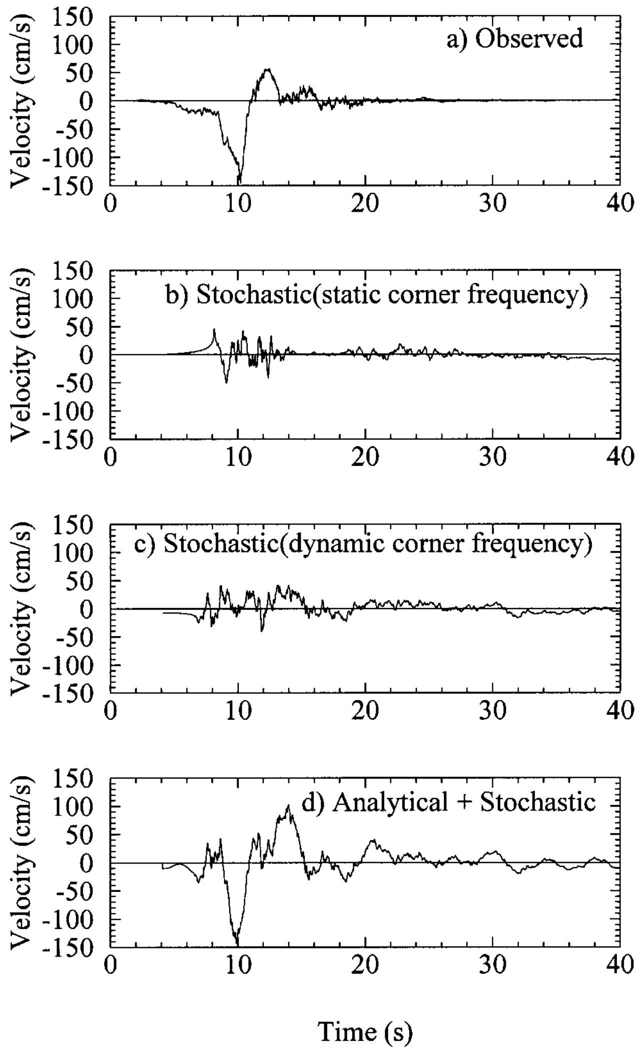

Figure 11. Recorded and simulated velocity time series for **M** 7.2, 1992 Landers earthquake (station LUC). The simulated times series are based on static and dynamic corner frequency approaches and a combination of the analytical and stochastic approach.

such as the LUC record from the Landers earthquake, the combination of the analytical and stochastic approach works well in producing realistic broadband time histories that match both low- and high-frequency motions.

The modifications offer several significant advantages over previous stochastic finite-fault models. First, there are conceptual advantages in that the new model does not depend on subfault size. The most frequent criticism of previous stochastic finite-fault models, including those by Schneider *et al.* (1993), Silva and Darragh (1995), and Beresnev and Atkinson (1998a, 2002), has been that the results depend on the selected subfault size. This constraint appears physically unrealistic and places constraints on the subfault sizes that may be used (e.g., the results will only match observations for a limited range of subfault size choices). We have demonstrated that, with the new model implementation, both the radiated energy and the ground motions are the same regardless of selected subfault size. Another conceptual advantage of our model is that it eliminates the need in previous approaches (Schneider *et al.*, 1993; Silva and Darragh, 1995; Beresnev and Atkinson, 1998a) to trigger each subfault several times to conserve seismic moment: our approach conserves moment with a single triggering of each subfault, which is more physically realistic.

Freed of the constraints on subfault size, our new approach is able to properly consider a wide range of magnitudes. In previous approaches, the minimum magnitude that could be simulated as a finite fault was about **M** 5 (Beresnev and Atkinson, 1999, 2002); the method broke down at smaller magnitudes because the prescribed subfault size approached the fault size. We are able to consider much smaller magnitudes. This has major advantages in applications in some regions. For example, in regions with few strong ground motion data, such as eastern North America, it is common to develop ground-motion relations by using a stochastic simulation model whose parameters are calibrated with seismographic data from small to moderate events (Atkinson and Boore, 1995; Toro *et al.*, 1997). In the past these simulations have been based on point-source models, which may not be appropriate when extended to large magnitudes. With the new approach introduced here, we can use a seamless finite-fault stochastic model to simulate ground motions from the smallest to the largest events of interest, using the small-event data to calibrate regional parameters such as attenuation and stress drop. Thus, the new stochastic finite-fault approach will aid in the development of ground-motion relations in data-poor regions.

Simulations based on the new EXSIM approach produce more realistic time series than those based on the previous stochastic finite-fault models implemented in the FINSIM model (Beresnev and Atkinson, 1998a). In FINSIM, the large subfault size that is required to model very large earthquakes (e.g., **M** 8) often produces artificial gaps in the simulated acceleration time series. With EXSIM, a small subfault size is chosen to eliminate any such artifacts in the time series.

The new model implements the concept of pulsing area behavior in stochastic finite-fault modeling. It is now generally accepted that the rise time of subfaults is much smaller than the duration of fault rupture (Heaton, 1990). Thus, a realistic model of fault rupture should allow for this behavior. Our initial model calibration for a suite of California earthquakes of **M** 5.0 to 7.3, suggesting that on average a maximum of 25% of the fault is slipping at any moment in time, implies that the percentage of pulsing area exerts an influence on ground-motion amplitudes in stochastic finite-fault modeling. Further studies will explore this behavior in more detail for specific earthquakes.

Finally, we have included the novel combination of analytical and stochastic methods proposed by Mavroeidis and Papageorgiou (2003) to provide a tool to describe the impulsive behavior of near-fault velocity pulses and their influence on long-period ground motions, as observed in many earthquakes. Thus, we provide a range of tools that cover the stochastic spectrum of finite-fault modeling and can be used to investigate the parameters that influence the characteristics of earthquake ground motion.

Acknowledgments

This study was supported by U.S. National Earthquake Hazards Reduction Program Grants 02HQGR0054 and 01HQPA0002 and by the Natural Sciences and Engineering Research Council of Canada. We thank David Boore, Kazuo Dan, Igor Beresnev, and an anonymous referee for stimulating discussion and comments.

References

Abrahamson, N., and W. Silva (1997). Empirical response spectral attenuation relations for shallow crustal earthquakes, *Seism. Res. Lett.* **68,** 94–127.

Aki, K. (1967). Scaling law of seismic spectrum, *J. Geophys. Res.* **72,** 1217–1231.

Aki, K., and P. Richards (1980). *Quantitative Seismology: Theory and Methods*, W. H. Freeman and Company, San Francisco.

Anderson, J., and S. Hough (1984). A model for the shape of the Fourier amplitude spectrum of acceleration at high frequencies, *Bull. Seism. Soc. Am.* **74,** 1969–1993.

Atkinson, G. (1984). Attenuation of strong ground motion in Canada from a random vibrations approach, *Bull. Seism. Soc. Am.* **74,** 2629–2653.

Atkinson, G., and D. Boore (1995). New ground motion relations for eastern North America, *Bull. Seism. Soc. Am.* **85,** 17–30.

Atkinson, G., and D. Boore (1997). Stochastic point-source modeling of ground motions in the Cascadia region, *Seism. Res. Lett.* **68,** 74–85.

Atkinson, G., and W. Silva (1997). Empirical source spectra for California earthquakes, *Bull. Seism. Soc. Am.* **87,** 97–113.

Atkinson, G., and W. Silva (2000). Stochastic modeling of California ground motions, *Bull. Seism. Soc. Am.* **90,** 255–274.

Berardi, R., M. Jimenez, G. Zonno, and M. Garcia-Fernandez (1999). Calibration of stochastic ground motion simulations for the 1997 Umbria-Marche, Central Italy, earthquake sequence, in *Proc. 9th Intl. Conf. On Soil Dynamics and Earthquake Engineering*, SDEE 99, August 1999, Bergen, Norway.

Beresnev, I., and G. Atkinson (1998a). FINSIM: a FORTRAN program for simulating stochastic acceleration time histories from finite faults, *Seism. Res. Lett.* **69,** 27–32.

Beresnev, I., and G. Atkinson (1998b). Stochastic finite-fault modeling of ground motions from the 1994 Northridge, California earthquake. I. Validation on rock sites, *Bull. Seism. Soc. Am.* **88,** 1392–1401.

Beresnev, I., and G. Atkinson (1999). Generic finite-fault model for ground motion prediction in eastern North America, *Bull. Seism. Soc. Am.* **89,** 608–625.

Beresnev, I., and G. Atkinson (2002). Source parameters of earthquakes in eastern and western North America based on finite-fault modeling, *Bull. Seism. Soc. Am.* **92,** 695–710.

Boatwright, J., and G. Choy (1992). Acceleration source spectra anticipated for large earthquakes in Northeastern North America, *Bull. Seism. Soc. Am.* **82,** 660–682.

Boore, D. (1983). Stochastic simulation of high-frequency ground motions based on seismological models of the radiated spectra, *Bull. Seism. Soc. Am.* **73,** 1865–1894.

Boore, D. (1996). SMSIM: Fortran programs for simulating ground motions from earthquakes, *U.S. Geol. Surv. Open-file Rept. 96-80-A*.

Boore, D., and G. Atkinson (1987). Stochastic prediction of ground motion and spectral response parameters at hard-rock sites in eastern North America, *Bull. Seism. Soc. Am.* **77,** 440–467.

Boore, D., and W. Joyner (1997). Site amplifications for generic rock sites, *Bull. Seism. Soc. Am.* **87,** 327–341.

Boore, D. M., W. B. Joyner, and L. Wennerberg (1992). Fitting the stochastic omega-squared source model to observed response spectra in Western North America: trade-offs between $\Delta\sigma$ and κ, *Bull. Seism. Soc. Am.* **82,** 1956–1963.

Brune, J. (1970). Tectonic stress and the spectra of seismic shear waves from earthquakes, *J. Geophys. Res.* **75,** 4997–5009.

Brune, J. (1971). Correction to J. Brune (1970), *J. Geophys. Res.* **76,** 5002.

Campbell, K. W. (1997). Empirical near-source attenuation relationships from horizontal and vertical components of peak ground acceleration, peak ground velocity, and pseudo-absolute acceleration response spectra, *Bull. Seism. Soc. Am.* **86,** 154–179.

Campillo, M., J.-C Gariel, K. Aki, and F. J. Sanchez-Sesma (1989). Destructive strong ground motion in Mexico City: source, path, and site effects during the Great 1985 Michoacan earthquake, *Bull. Seism. Soc. Am.* **79,** 1718–1735.

Hanks, T. (1975). Strong ground motion of the San Fernando, California, earthquake: ground displacements, *Bull. Seism. Soc. Am.* **65,** 193–225.

Hanks, T., and R. McGuire (1981). The character of high-frequency strong ground motion, *Bull. Seism. Soc. Am.* **71,** 2071–2095.

Hartzell, S. (1978). Earthquake aftershocks as Green's functions, *Geophys. Res. Lett.* **5,** 1–14.

Hartzell, S., S. Harmsen, A. Frankel, and S. Larsen (1999). Calculation of broadband time histories of ground motion: comparison of methods and validation using strong-ground motion from the 1994 Northridge earthquake, *Bull. Seism. Soc. Am.* **89,** 1484–1504.

Heaton, T. (1990). Evidence for and implications of self-healing pulses of slip in earthquake rupture, *Phys. Earth Planet. Interiors* **64,** 1–20.

Heaton, T., and S. Hartzell (1986). Source characteristics of hypothetical subduction earthquakes in the Northwestern United States, *Bull. Seism. Soc. Am.* **76,** 675–708.

Hirasawa, T., and W. Stauder (1965). On the seismic body waves from a finite moving source, *Bull. Seism. Soc. Am.* **55,** 237–262.

Hough, S., and D. Dreger (1995). Source parameters of the 23 April 1992 M 6.1 Joshua Tree, California, earthquake and its aftershocks: empirical Green's function analysis of GEOS and TERRAscope data, *Bull. Seism. Soc. Am.* **85,** 1576–1590.

Irikura, K. (1983). Semi-empirical estimation of strong ground motions during large earthquakes, *Bull. Disaster Prev. Res. Inst. Kyoto Univ.* **33,** 63–104.

Joyner, W. (1984). A scaling law for the spectra of large earthquakes, *Bull. Seism. Soc. Am.* **74,** 1167–1188.

Joyner, W. (2000). Strong motion from surface waves in deep sedimentary basins, *Bull. Seism. Soc. Am.* **90,** S95–S112.

Joyner, W., and D. Boore (1986). On simulating large earthquakes by Green's function addition of smaller earthquakes, in *Earthquake Source Mechanics*, American Geophysical Monograph **37,** 269–274.

Joyner, W. B., and D. M. Boore (1988). Measurement, characterization, and prediction of strong ground motion, in *Earthquake Engineering and Soil Dynamics II, Proc. Am. Soc. Civil Eng. Geotech. Eng. Div. Specialty Conference*, 27–30 June 1988, Park City, Utah, 43–102.

Liu, H. L., and T. H. Heaton (1984). Array analysis of the ground velocities and accelerations from the 1971 San Fernando, California, earthquake, *Bull. Seism. Soc. Am.* **74,** 1951–1968.

Margaris, B., and D. Boore (1998). Determination of $\Delta\sigma$ and κ_0 from response spectra of large earthquakes in Greece, *Bull. Seism. Soc. Am.* **88,** 170–182.

Mavroeidis, G. P., and A.S. Papageorgiou (2002). Near-source strong ground motion: characteristics and design issues, in *Proc. of the Seventh U.S. National Conf. on Earthquake Engineering (7NCEE)*, Boston, Massachusetts, 21–25 July 2002.

Mavroeidis, G. P., and A. S. Papageorgiou (2003). A mathematical representation of near-fault ground motions, *Bull. Seism. Soc. Am.* **93,** 1099–1131.

Miyake, H., T. Iwata, and K. Irikura (2003). Source characterization for broadband ground-motion simulation: kinematic heterogeneous source model and strong motion generation area, *Bull Seism. Soc. Am.* **93,** 2531–2545.

Motazedian, D. (2004). California ground motions from a hybrid finite fault model, *J. Geophys. Res.*, 61–80.

Ou, G., and R. Herrmann (1990). A statistical model for peak ground motion from local to regional distances, *Bull. Seism. Soc. Am.* **80,** 1397–1417.

Papageorgious, A. S. (1998). The character of near-source ground motions and related seismic design, in *Proc of the Structural Engineers World Congress*, San Francisco, California, 18–23 July 1998.

Pitarka, A., P. Somerville, Y. Fukushima, and T. Uetake (2002). Ground motion attenuation from the 1995 Kobe earthquake based on simulations using the hybrid Green's function method, *Bull. Seism. Soc. Am.* **92,** 1025–1031.

Pitarka, A., P. Somerville, Y. Fukushima, T. Uetake, and K. Irikura (2000). Simulation of near-fault strong-ground motion using hybrid Green's functions, *Bull. Seism. Soc. Am.* **90,** 566–586.

Rovelli, A., A. Caserta, L. Malignini, and F. Marra (1994). Assessment of potential strong motions in the city of Rome, *Ann. Geofis.* **37,** 1745–1769.

Rovelli, A., M. Cocco, R. Console, B. Alessandrini, and S. Mazza (1991). Ground motion waveforms and source spectral scaling from close-distance accelerograms in a compressional regime area (Friuli, northeastern Italy), *Bull. Seism. Soc. Am.* **81,** 57–80.

Schneider, J., W. Silva, and C. Stark (1993). Ground motion model for the 1989 M 6.9 Loma Prieta earthquake including effects of source, path and site, *Earthquake Spectra* **9,** 251–287.

Silva, W., and R. Darragh (1995). Engineering characterization of strong ground motion recorded at rock sites, Electric Power Res. Inst. Rept. TR-102262.

Silva, W. J., I. G. Wong, and R. B. Darragh (1991). Engineering characterization of earthquake strong ground motions with applications to the Pacific northwest, *U.S. Geol. Surv. Open-file Rept. 91-441-H*.

Singh, S. K., M. Ordaz, J. G. Anderson, M. Rodriguez, R. Quaas, E. Mena, M. Ottaviani, and D. Almora (1989). Analysis of near-source strong-motion recordings along the Mexican subduction zone, *Bull. Seism. Soc. Am.* **79,** 1697–1717.

Sokolov, V. (1997). Empirical models for estimating Fourier-amplitude spectra of ground acceleration in the Northern Caucasus (Racha Seismogenic Zone), *Bull. Seism. Soc. Am.* **87,** 1401–1412.

Somerville, P. (1998). Development of an improved representation of near-fault ground motions, SMIP98-CDMG, Oakland, California, 1–20.

Somerville, P. (2000). New development in seismic hazard estimation, in *Proc. of the Sixth Int. Conf. on Seismic Zonation (6ICSZ)*, Palm Springs, California, 12–15 November 2000.

Somerville, P., M. Sen, and B. Cohee (1991). Simulations of strong ground motions recorded during the 1985 Michoacan, Mexico and Valparaiso, Chile, earthquakes, *Bull. Seism. Soc. Am.* **81,** 1–27.

Somerville., P., N. C. Smith, and R. W. Graves (1997). Modification of Empirical Strong Ground Motion Attenuation Relations to Include the Amplitude and Duration Effects of Rupture Directivity, *Seism. Res. Lett.* **68,** no. 1, 199–221.

Toro, G., and R. McGuire (1987). An investigation into earthquake ground motion characteristics in eastern North America, *Bull. Seism. Soc. Am.* **77,** 468–489.

Toro, G., N. Abrahamson, and J. Schneider (1997). Model of strong ground motion in eastern and central North America: best estimates and uncertainties, *Seism. Res. Lett.* **68,** 41–57.

Tumarkin, A., and R. Archuleta (1994). Empirical ground motion prediction, *Ann. Geofis.* **37,** 1691–1720.

Vidale, J. E., and D. V. Helmberger (1988). Elastic finite-difference modeling of the 1971 San Fernando, California earthquake, *Bull. Seism. Soc. Am.* **78,** 122–141.

Wald, D. J., T. H. Heaton, and K. W. Hudnut (1996). The slip history of the 1994 Northridge, California, Earthquake determined from strong motion, teleseismic, GPS, and leveling data, *Bull. Seism. Soc. Am.* **86,** S49–S70.

Wells, D., and K. Coppersmith (1994). New empirical relationships among magnitude, rupture length, rupture width, rupture area, and surface displacement, *Bull. Seism. Soc. Am.* **84,** 974–1002.

Zeng, Y., J. Anderson, and G. Yu (1994). A composite source model for computing realistic synthetic strong ground motions, *Geophys. Res. Lett.* **21,** 725–728.

Department of Earth Science
Carleton University
Ottawa, Ontario K1S5B6, Canada
gma@ccs.carleton.ca
dariush@ccs.carleton.ca
www.carleton.ca/~dariush

Manuscript received 10 October 2003.